Journal of Luminescence 194 (2018) 131–138

Contents lists available at ScienceDirect

Journal of Luminescence

journal homepage: www.elsevier.com/locate/jlumin

Synthesis and narrow red luminescence of $Cs_2HfF_6:Mn^{4+}$, a new phosphor for warm white LEDs

Tim Senden*, Elleke J. van Harten, Andries Meijerink

Condensed Matter and Interfaces, Debye Institute for Nanomaterials Science, Utrecht University, P.O. Box 80000, 3508 TA Utrecht, The Netherlands

ARTICLE INFO

Keywords:
Mn^{4+}
Fluorohafnate
White LED
Red phosphor

ABSTRACT

Mn^{4+}-doped fluorides show narrow red line emission under blue light excitation and are therefore promising materials to improve the color rendering and luminous efficacy of white light emitting diodes (wLEDs). The synthesis of Mn^{4+}-doped fluorides is however challenging and so far only a few efficient Mn^{4+}-doped fluoride phosphors have been reported. In this work we present the synthesis and optical properties of a novel $Cs_2HfF_6:Mn^{4+}$ phosphor. The $Cs_2HfF_6:Mn^{4+}$ phosphor is prepared via a two-step co-precipitation method and shows bright red Mn^{4+} luminescence around 620 nm under blue light excitation. Detailed insight in the luminescence properties is obtained by studying the Mn^{4+} emission and luminescence decay down to cryogenic temperatures. The $Cs_2HfF_6:Mn^{4+}$ phosphor has a photoluminescence quantum efficiency higher than 80%, which makes it an interesting red-emitting material for wLEDs and other lighting applications. As the Mn^{4+} emission from $Cs_2HfF_6:Mn^{4+}$ shows quenching above 100 °C ($T_{½}$ = 403 K), the use of this phosphor will be limited to low-power LED lighting.

1. Introduction

White light emitting diodes (wLEDs) are revolutionizing the display and lighting industry due to their high energy efficiency, small size, robustness and long operation lifetime [1–5]. Most commercial high efficiency wLEDs are based on a combination of blue emitting (In,Ga)N LED chips and yellow emitting $Y_3Al_5O_{12}:Ce^{3+}$ (YAG:Ce) phosphors [5–8]. This combination however lacks a red emitting component and thus gives "cool" white light with a high correlated color temperature (CCT > 4500 K) and low color rendering index (CRI < 75). This is an issue for most applications including home lighting where warm white light with a high color rendering index (CRI > 85) is required. To solve this problem, the last two decades extensive research has been conducted to find novel red phosphors that can improve the color rendering of wLEDs. Presently Eu^{2+}-doped nitrides like $CaAlSiN_3:Eu^{2+}$ are the most successful red-emitting LED phosphors [9–14] and warm wLEDs containing these nitrides have been commercialized in the last years.

Eu^{2+}-doped nitride phosphors exhibit high photoluminescence quantum efficiencies (QE > 90%), good thermal quenching behavior and sufficient chemical stability [2,5] but also have several serious drawbacks. The Eu^{2+} emission band of these phosphors is broad (full width at half maximum fwhm = 50–90 nm) and therefore extends into the deep-red spectral region (λ > 640 nm) where the eye sensitivity is low. This causes the lumen/W efficacy of the wLED to reduce significantly [7]. Furthermore, Eu^{2+}-doped nitride phosphors have a high production cost as they are synthesized under demanding conditions such as high pressure and high temperature [14,15]. Hence, the wLED industry is searching for new cheap and efficient narrow linewidth (fwhm < 40 nm) red phosphors that can be excited by blue LEDs. Red emitting phosphors with these spectral characteristics could enable lighting systems with an increased lumen/W efficacy at a CRI of 90 or higher.

Fluoride compounds doped with Mn^{4+} ($3d^3$ electron configuration) ions show narrow red emission (fwhm < 30 nm) in a favorable spectral region (λ_{max} ~ 630 nm). Moreover, their red emission can be excited by blue light and they are therefore promising narrow linewidth red phosphors for wLEDs [16–19]. Mn^{4+}-doped fluoride phosphors can have quantum efficiencies higher than 90% [15,20] and, in contrast to the Eu^{2+}-doped nitrides, are prepared through low-cost wet-chemical synthesis at room temperature [15,21,22]. These properties give Mn^{4+}-doped fluoride phosphors large potential for application and consequently the synthesis of these phosphors has received considerable attention in recent years. The synthesis of Mn^{4+}-doped compounds is however not trivial and up till now only a few Mn^{4+}-doped fluoride hosts have been reported [19]. The many oxidation states of manganese (2+, 3+, 4+ and 7+ are most common) make it difficult to control the valence state of manganese and thereby to synthesize Mn^{4+}-doped

* Corresponding author.
E-mail address: t.senden@uu.nl (T. Senden).

http://dx.doi.org/10.1016/j.jlumin.2017.10.006
Received 11 August 2017; Received in revised form 26 September 2017; Accepted 2 October 2017
Available online 05 October 2017

compounds. Another issue is that manganese oxide impurities are often formed when synthesizing Mn^{4+}-doped fluorides [22,23]. Furthermore, Mn^{4+} ions substitute preferably for octahedrally coordinated tetravalent cations, which makes it challenging to activate most fluoride lattices with Mn^{4+} ions. As a result, only a small number of Mn^{4+}-doped fluorides has been synthesized so far. All fluoride hosts activated with Mn^{4+} ions contain either Si^{4+}, Ti^{4+}, Ge^{4+}, Sn^{4+}, Zr^{4+} or Al^{3+} as their central cation [24,25]. Substitution of Mn^{4+} for other metal ions has so far not been achieved in fluorides.

In this work we report the synthesis and luminescence properties of a new Mn^{4+}-activated fluoride host: a Mn^{4+}-doped fluorohafnate. We synthesize a novel Cs_2HfF_6:Mn^{4+} phosphor, which was also recently reported by Yang et al. [26]. In their work Cs_2HfF_6:Mn^{4+} was prepared via an ion exchange method. In contrast, here we use a two-step co-precipitation method to synthesize Cs_2HfF_6:Mn^{4+}. In a first step we prepare the Mn^{4+}-precursor K_2MnF_6 and then in a second step Cs_2HfF_6:Mn^{4+} is precipitated from an aqueous HF solution containing Cs^+, Hf^{4+} and Mn^{4+} ions. The method described here results in narrow red-emitting Cs_2HfF_6:Mn^{4+} phosphors with luminescence quantum efficiencies of 80–90%, which is much higher than the 50–60% quantum efficiency reported for Cs_2HfF_6:Mn^{4+} by Yang et al. [26]. In Ref. [26] the optical properties of Cs_2HfF_6:Mn^{4+} were briefly described. In this work we provide detailed insight in the optical properties by recording emission and excitation spectra at cryogenic temperatures. The low-temperature spectra are used to accurately determine the energies of the Mn^{4+} levels and MnF_6^{2-} vibrational modes and the crystal field and Racah parameters. Furthermore we study the thermal quenching behavior for Cs_2HfF_6:Mn^{4+} by measuring the luminescence intensity and luminescence decay times as function of temperature. Because of luminescence quenching above 100 °C, application of this Mn^{4+}-doped fluorohafnate will be limited to low-power LED systems.

2. Experimental section

2.1. Synthesis of K_2MnF_6

K_2MnF_6 was prepared according to the procedure described in Refs. [27,28]. Briefly, 60 g of KF and 4 g of $KMnO_4$ were dissolved in 250 mL of a 40 wt% HF solution. The solution was cooled with an ice bath and stirred for 30 min. Next, 4.5 mL of a 30 wt% H_2O_2 solution was added dropwise while stirring which resulted in the gradual precipitation of yellow K_2MnF_6 powder. The dropwise addition of H_2O_2 was stopped when the color of the solution turned from purple to red-brown indicating the formation of Mn^{4+}. K_2MnF_6 was isolated by decanting the red-brown solution, washing the precipitate twice with 100 mL of acetone and subsequently drying at 50 °C for 2 h.

2.2. Synthesis of Cs_2HfF_6:Mn^{4+} phosphor

The Cs_2HfF_6:Mn^{4+} phosphor was synthesized by a simple co-precipitation method which is schematically illustrated in Fig. 1a. First, 10 mmol of HfO_2 was dissolved in 100 mL of a 40 wt% HF solution by stirring at 60 °C for 24 h. Subsequently, 0.2 mmol of K_2MnF_6 and a solution of 20 mmol CsF in 3 mL 40 wt% HF were added. The solution became yellow due to the addition of K_2MnF_6. The solution was stirred for several minutes and then poured into 200 mL of ethanol which resulted in the precipitation of Cs_2HfF_6:Mn^{4+} phosphor particles. The precipitate was washed with ethanol and dried at 75 °C for 2 h. The Cs_2HfF_6:Mn^{4+} phosphor has a yellow-orange body color under daylight (Fig. 1b) and shows bright red luminescence under UV light illumination (Fig. 1c).

2.3. Characterization

Powder X-ray diffraction (XRD) patterns were measured on a Philips PW1729 x-ray diffractometer using Cu K_α radiation (λ = 1.5418 Å). Scanning electron microscopy (SEM) images and energy-dispersive X-ray (EDX) spectra of the phosphors were obtained using a Philips XL30S FEG microscope operating at 20 keV. The manganese concentration in the synthesized Cs_2HfF_6:Mn^{4+} phosphor was determined with inductively coupled plasma optical emission spectroscopy (ICP-OES) performed on a Perkin-Elmer Optima 8300DV spectrometer. For the ICP-OES measurements the Cs_2HfF_6:Mn^{4+} phosphor was dissolved in aqua regia.

Photoluminescence (PL) measurements were performed on an Edinburgh Instruments FLS920 fluorescence spectrometer. Excitation and emission spectra were recorded with a 450 W Xe lamp as excitation source and a Hamamatsu R928 photomultiplier tube (PMT) with a grating blazed at 500 nm for detection of emission. For PL decay measurements excitation was done with a tunable optical parametric oscillator (OPO) Opotek Opolette HE 355II laser (pulse width 10 ns, repetition rate 10 Hz) and emission was detected with a Hamamatsu H74220-60 PMT. Samples were cooled down to 4 K with an Oxford Instruments liquid helium flow cryostat. For PL measurements between 300 and 600 K samples were heated in a Linkam THMS600 temperature controlled stage. The PL quantum efficiency of the phosphor was determined with a calibrated home-built setup which consisted of a 65 W Xe lamp, excitation monochromator, integrating sphere (Labsphere) and CCD camera (Avantes AvaSpec-2048).

3. Results and discussion

3.1. Structural characterization of phosphor particles

To investigate the phase purity, size, shape and composition of the Cs_2HfF_6:Mn^{4+} phosphor particles, we employed different characterization methods such as powder x-ray diffraction (XRD), scanning electron microscopy (SEM), energy-dispersive x-ray (EDX) spectroscopy and inductively coupled plasma optical emission spectroscopy (ICP-OES). Fig. 2a shows the XRD pattern of the Cs_2HfF_6:Mn^{4+} phosphor. The XRD pattern is in excellent agreement with the reference pattern of trigonal Cs_2HfF_6 (PDF 04-008-3370). No impurity crystal phases are observed. The trigonal crystal structure of Cs_2HfF_6 ($P\bar{3}m1$ space group) [29] is displayed in Fig. 2b. Each Hf^{4+} ion is surrounded by six F^- ions to form a trigonally distorted HfF_6^{2-} octahedron (accentuated in Fig. 2b). The distorted HfF_6^{2-} octahedron has a D_{3d} symmetry with Hf–F distances of 2.03 Å.

Fig. 2c,d shows SEM images of Cs_2HfF_6:Mn^{4+} phosphor particles. The particles have irregular shapes and are very polydisperse, with sizes ranging from 100 nm to 100 μm. We attribute this to fast and forced crystallization in the anti-solvent ethanol. If the Cs_2HfF_6:Mn^{4+} phosphor would be formed by slowly evaporating the HF solution, monodisperse particles with a hexagonal shape may be obtained based on the trigonal crystal structure of Cs_2HfF_6. EDX spectroscopy measurements (Fig. S1) confirm that the Cs_2HfF_6:Mn^{4+} phosphor particles shown in Fig. 2c,d consist of cesium, hafnium and fluorine ions. All intense peaks in the EDX spectrum can be assigned to K, L or M x-ray emission lines of these elements. The manganese concentration in the particles is too low to be detected by EDX spectroscopy. Hence, we used ICP-OES as technique to determine the manganese concentration in the Cs_2HfF_6:Mn^{4+} phosphor. It was found that the Cs_2HfF_6:Mn^{4+} phosphor contains 1.9 mol% of manganese ions, which is close to the 2.0 mol% of K_2MnF_6 added during the synthesis. In the work of Yang et al. less than 60% of the Mn^{4+} added in the synthesis ended up in the phosphor crystals [26]. Our method thus gives better control over the incorporation of Mn^{4+} ions in the Cs_2HfF_6 host lattice.

3.2. Red Mn^{4+} luminescence of Cs_2HfF_6:Mn^{4+}

Upon illumination with UV radiation Cs_2HfF_6:Mn^{4+} shows bright red luminescence, as can be seen in Fig. 1c. To investigate this luminescence, we measured photoluminescence (PL) excitation and

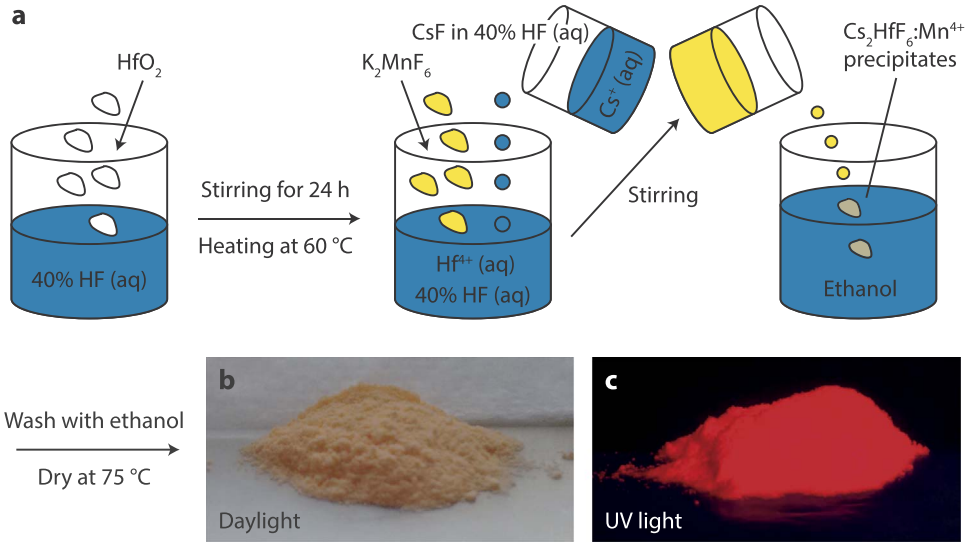

Fig. 1. (a) Schematic illustration of the synthesis of $Cs_2HfF_6:Mn^{4+}$ and photographic images of $Cs_2HfF_6:Mn^{4+}$ phosphor under (b) daylight and (c) 365 nm UV illumination.

emission spectra of $Cs_2HfF_6:Mn^{4+}$ at room temperature. These spectra are presented in Fig. 3a. $Cs_2HfF_6:Mn^{4+}$ shows narrow emission lines around 620 nm under blue light excitation (λ_{exc} = 470 nm). The main emission peaks are in the wavelength range of 610–640 nm where eye sensitivity is still relatively high, which is beneficial for applications. The red luminescence is assigned to the Mn^{4+} $^2E \rightarrow {}^4A_2$ transition, which is indicated by the red arrow in the Tanabe–Sugano energy level diagram of Mn^{4+} ($3d^3$) in Fig. 3b. The Tanabe–Sugano diagram [30,31] depicts the energy levels of the d^3 electron configuration in an octahedral crystal field as a function of the crystal field splitting Δ_O. Due to its high effective charge, the Mn^{4+} ion experiences a strong crystal field and therefore the ^2E state is generally the lowest energy excited state. The ^2E excited state and $^4A_2$ ground state have the same t_2^3 configuration and as a result the energy of the $^2E \rightarrow {}^4A_2$ transition hardly depends on Δ_O. Consequently, there is little to no lateral displacement between the parabolas of the ^2E and $^4A_2$ state (small Huang–Rhys parameter [32]) causing the $^2E \rightarrow {}^4A_2$ emission to be characterized by narrow zero-phonon and vibronic emission lines.

The emission spectrum of $Cs_2HfF_6:Mn^{4+}$ is displayed in more detail in Fig. 3c. The spectrum shows a weak line at 622 nm symmetrically surrounded by lines at shorter and longer wavelengths. This resembles emission spectra observed for other Mn^{4+}-doped fluorides such as $K_2SiF_6:Mn^{4+}$ and $K_2TiF_6:Mn^{4+}$ [17,33]. In analogy, the $^2E \rightarrow {}^4A_2$ spectrum of $Cs_2HfF_6:Mn^{4+}$ consists of a weak zero-phonon line (ZPL) at ~ 622 nm and more intense anti-Stokes and Stokes vibronic emissions (labeled ν_3, ν_4 and ν_6) on the high and low energy side of the ZPL, respectively. In $Cs_2HfF_6:Mn^{4+}$ the $^2E \rightarrow {}^4A_2$ electric dipole transition is forbidden because Mn^{4+} is located on a site with inversion symmetry (Hf^{4+} site with D_{3d} symmetry). As a consequence, the zero-phonon emission (ZPL) is very weak (see Fig. 3c). The transition however gains intensity by coupling to asymmetric (*ungerade*) vibrational modes in the MnF_6^{2-} center [34,35]. Asymmetric vibrational modes induce odd-parity crystal field terms that mix some odd-parity states into the even-parity (*gerade*) Mn^{4+} $3d^3$ states (in $Cs_2HfF_6:Mn^{4+}$ all $3d^3$ states have *gerade* symmetry as Mn^{4+} is located on a site with inversion symmetry). Due to this mixing the $^2E \rightarrow {}^4A_2$ transition becomes partly electric dipole allowed. The vibrational modes of the MnF_6^{2-} ion that have ungerade symmetry are the $\nu_3(T_{1u})$, $\nu_4(T_{1u})$ and $\nu_6(T_{2u})$ modes [36,37]. Hence, the most intense emission lines in Fig. 3c are assigned to $^2E \rightarrow {}^4A_2$ transitions coupling with these vibrations. Thermal population of these phonon modes at room-temperature allows the transition to couple with phonons in the excited state (giving rise to the anti-Stokes

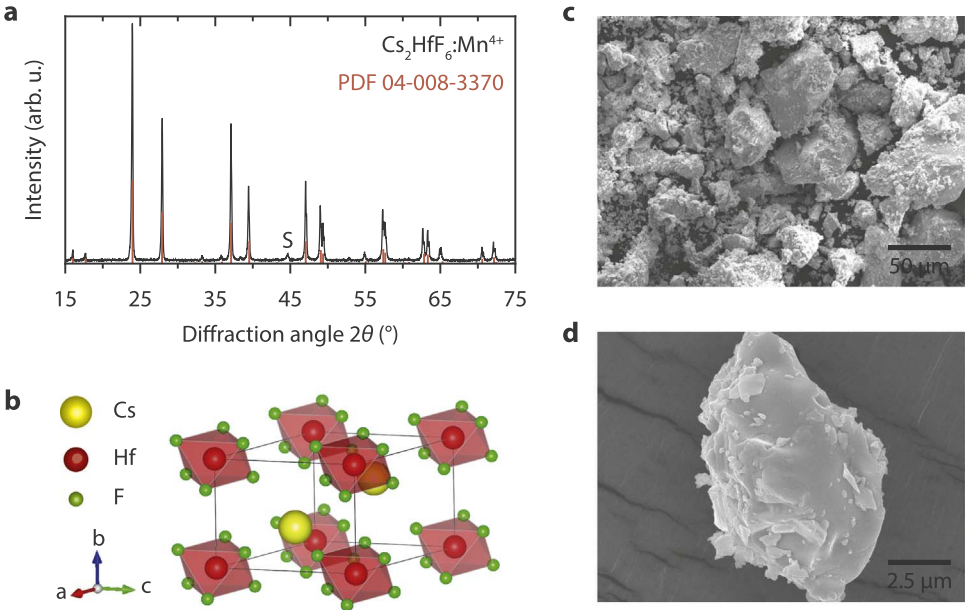

Fig. 2. (a) Powder X-ray diffraction (XRD) pattern of $Cs_2HfF_6:Mn^{4+}$ (black) and reference pattern of Cs_2HfF_6 (red lines, PDF 04-008-3370). The S marks a diffraction peak originating from the aluminum sample holder. (b) Crystal structure of Cs_2HfF_6 ($P\bar{3}m1$ space group). The distorted HfF_6^{2-} octahedra have been accentuated. (c,d) SEM images of $Cs_2HfF_6:Mn^{4+}$ phosphor particles. (For interpretation of the references to color in this figure legend, the reader is referred to the web version of this article.).

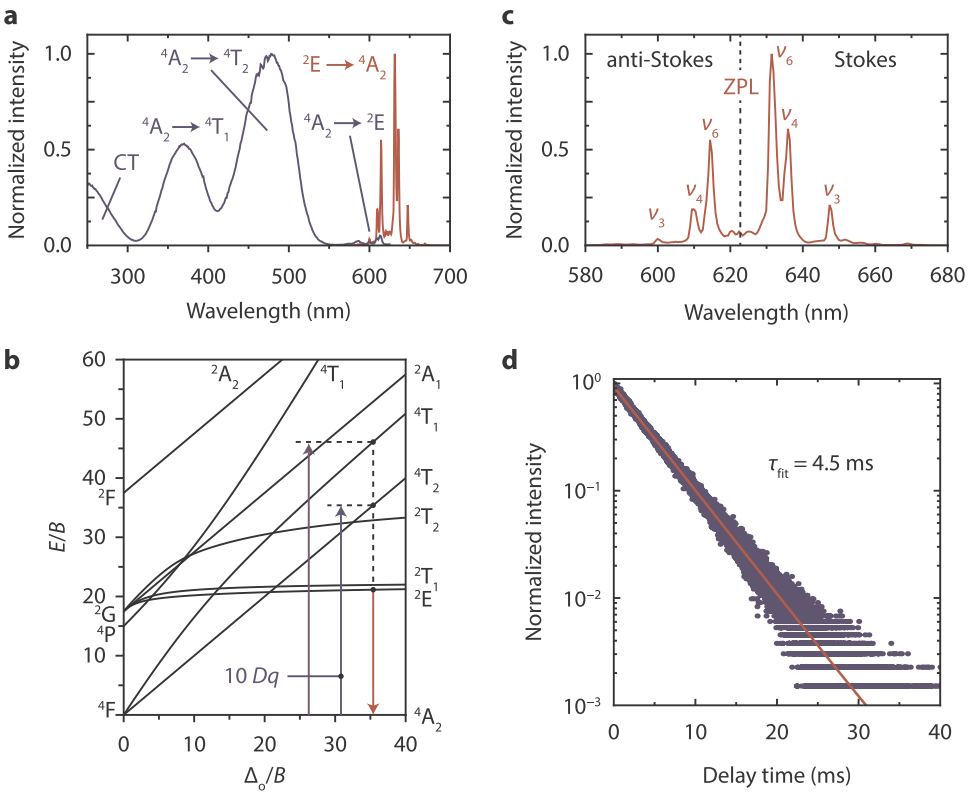

Fig. 3. (a) Room-temperature PL excitation (blue, λ_{em} = 632 nm) and emission (red, λ_{exc} = 470 nm) spectra of $Cs_2HfF_6:Mn^{4+}$ (1.9%). The emission and excitation bands/lines are assigned to corresponding transitions in the d^3 Tanabe-Sugano diagram. (b) Tanabe-Sugano energy level diagram of the d^3 electron configuration in an octahedral crystal field (C = 4.5B). The $^4A_2 \rightarrow {}^4T_1$, $^4A_2 \rightarrow {}^4T_2$ and $^2E \rightarrow {}^4A_2$ transitions of Mn^{4+} are indicated by the purple, blue and red arrows, respectively. Note that the excitation transitions are displaced for clarity. For a specific coordination all transitions take place around the same crystal field. The energy of the $^4A_2 \rightarrow {}^4T_2$ transition equals the crystal field splitting Δ_O (or 10 Dq). (c) Enlarged emission spectrum showing the zero-phonon line (ZPL) and (anti-)Stokes vibronic $^2E \rightarrow {}^4A_2$ emissions of $Cs_2HfF_6:Mn^{4+}$. (d) PL decay curve of the Mn^{4+} emission in $Cs_2HfF_6:Mn^{4+}$ (1.9%) (λ_{exc} = 470 nm, λ_{em} = 632 nm and T = 298 K). The decay time corresponding to the mono-exponential fit (red line) is 4.5 ms. (For interpretation of the references to color in this figure legend, the reader is referred to the web version of this article.).

lines) while transitions to these phonon modes in the ground state can occur at all temperatures (Stokes lines). As a result, both anti-Stokes and Stokes vibronic emissions are observed in the room temperature PL spectrum.

To further understand the luminescence properties of Mn^{4+} in Cs_2HfF_6 we analyze the positions of the Mn^{4+} excitation bands. The red Mn^{4+} luminescence of $Cs_2HfF_6:Mn^{4+}$ has two broad excitation bands with maxima at 367 and 477 nm, respectively (Fig. 3a). These bands are assigned to the Mn^{4+} $^4A_2 \rightarrow {}^4T_1$ (^4F) and $^4A_2 \rightarrow {}^4T_2$ transitions (violet and blue arrows in Tanabe-Sugano diagram in Fig. 3b). The $^4A_2 \rightarrow {}^4T_2$ excitation band shows good overlap with the blue emission of (In,Ga)N LED chips. At wavelengths shorter than 300 nm, another broad excitation band is visible. This band is assigned to the $F^- \rightarrow Mn^{4+}$ charge-transfer (CT) transition [15,34]. Besides the broad $^4A_2 \rightarrow {}^4T_1$, $^4A_2 \rightarrow {}^4T_2$ and $F^- \rightarrow Mn^{4+}$ CT excitation bands, the PL excitation spectrum exhibits some weak excitation lines around 600 nm which are assigned to Mn^{4+} $^4A_2 \rightarrow {}^2E$ and $^4A_2 \rightarrow {}^2T_1$ transitions. These transitions are spin-forbidden and therefore low in intensity relative to the spin-allowed $^4A_2 \rightarrow {}^4T_1$ and $^4A_2 \rightarrow {}^4T_2$ transitions. Since the $^4T_1$ and $^4T_2$ states have a different electron configuration than the $^4A_2$ ground state (t_2^3e versus t_2^3), there is an offset between the potential curve equilibrium positions of the $^4A_2$ ground state and the $^4T_{1,2}$ excited states. As a consequence, the $^4A_2 \rightarrow {}^4T_1$ and $^4A_2 \rightarrow {}^4T_2$ excitation bands are broad (large Huang-Rhys parameter [32]) and their transition energies are sensitive to the strength of the crystal field (see Fig. 3b). If we compare the energy of the $^4A_2 \rightarrow {}^4T_2$ excitation band in $Cs_2HfF_6:Mn^{4+}$ to the energy of this band in other Mn^{4+}-doped fluoride phosphors, we see the influence of the crystal field splitting on the $^4T_2$ and $^4T_1$ levels. In $Cs_2HfF_6:Mn^{4+}$ the maximum of the $^4A_2 \rightarrow {}^4T_2$ band is at 477 nm, where e.g. for $K_2SiF_6:Mn^{4+}$ it is centered around 450 nm [17,34]. The ionic radius of Hf^{4+} (r = 0.71 Å) is significantly larger than the ionic radius of Si^{4+} (r = 0.40 Å) [38] and therefore the Mn–F distance is longer in $Cs_2HfF_6:Mn^{4+}$. This results in a weaker crystal field splitting, causing the $^4T_2$ state to be at lower energy in $Cs_2HfF_6:Mn^{4+}$ when compared to $K_2SiF_6:Mn^{4+}$.

For applications in lighting it is important that the luminescence of $Cs_2HfF_6:Mn^{4+}$ has a high PL quantum efficiency (QE). The QE is defined as the ratio between the number of emitted and absorbed photons. We measured the QE of several $Cs_2HfF_6:Mn^{4+}$ phosphor samples by using a calibrated set-up with an integrating sphere (see Experimental Section). The $Cs_2HfF_6:Mn^{4+}$ phosphors presented in this work exhibit quantum efficiencies of 80–90% and therefore have a much higher QE than the $Cs_2HfF_6:Mn^{4+}$ phosphors reported by Yang et al. [26], which showed a QE of ~60%. The high QE of 80–90% gives $Cs_2HfF_6:Mn^{4+}$ large potential for application, especially since so far no optimization of the synthesis method has been done. Given that the QE is very high, it is expected that the PL decay of the Mn^{4+} emission is mainly radiative. The PL decay curve of $Cs_2HfF_6:Mn^{4+}$ in Fig. 3d shows a mono-exponential decay, confirming the decay of the ^2E excited state is mainly radiative. The fitted decay time is 4.5 ms, which is a typical radiative lifetime for the parity- and spin-forbidden $^2E \rightarrow {}^4A_2$ transition of Mn^{4+}. The Mn^{4+} emission lifetime of $Cs_2HfF_6:Mn^{4+}$ is shorter than the lifetime of most other Mn^{4+}-doped fluorides, which usually exhibit an emission lifetime of 5–8 ms [19,24]. An explanation for the shorter ^2E lifetime in $Cs_2HfF_6:Mn^{4+}$ is the stronger relaxation of the spin selection rule by admixture of the $^4T_2$ excited state into the ^2E excited state through spin-orbit coupling. Due to the low position of the $^4T_2$ state in $Cs_2HfF_6:Mn^{4+}$, the ^2E-$^4T_2$ gap is small and the mixing of $^4T_2$ into ^2E through spin-orbit coupling will be stronger compared to other Mn^{4+}-doped fluorides.

3.3. Energies of the Mn^{4+} levels and vibrational modes

To accurately determine the energies of the Mn^{4+} levels in $Cs_2HfF_6:Mn^{4+}$, we recorded and analyzed high-resolution PL spectra for $Cs_2HfF_6:Mn^{4+}$ at T = 4 K. At cryogenic temperatures there is less thermal broadening of emission and excitation bands and therefore zero-phonon lines (ZPLs) may be observed. These lines give the energies of the purely electronic transitions to the Mn^{4+} excited states. Furthermore, with reduced thermal broadening we can study the vibronic fine structure of the Mn^{4+} emission and excitation bands and thereby obtain the vibrational energies of the MnF_6^{2-} group.

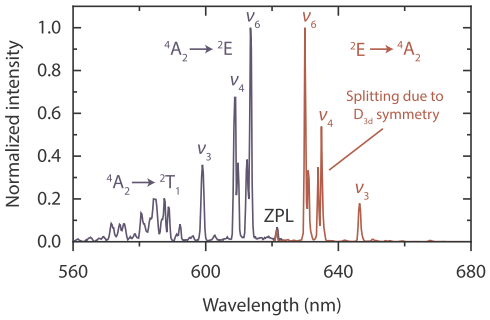

Fig. 4. PL excitation (blue, λ_{em} = 630 nm) and emission (red, λ_{exc} = 472 nm) spectra of $Cs_2HfF_6:Mn^{4+}$ at T = 4 K. For the excitation spectrum only the spectral region of the $^4A_2 \rightarrow {}^2T_1$ and $^4A_2 \rightarrow {}^2E$ transitions is shown. The ν_4 and ν_6 excitation and emission lines show a splitting due to the D_{3d} site symmetry for Mn^{4+} in $Cs_2HfF_6:Mn^{4+}$.

Fig. 4 shows low-temperature (T = 4 K) spectra of the $^2E \rightarrow {}^4A_2$ emission and $^4A_2 \rightarrow {}^2T_1$,$^2E$ excitations of $Cs_2HfF_6:Mn^{4+}$. In the emission spectrum we observe the ZPL of the $^2E \rightarrow {}^4A_2$ transition at 621.4 nm, which means the energy of the ^2E level is 16,093 cm^{-1}. As expected the ZPL of the opposite $^4A_2 \rightarrow {}^2E$ transition is found at the same energy in the excitation spectrum. The ^2E energy of $Cs_2HfF_6:Mn^{4+}$ is similar to the ^2E energies observed for other Mn^{4+}-doped fluorides [18,39].

In line with the luminescence properties at room temperature, the 4 K emission spectrum of $Cs_2HfF_6:Mn^{4+}$ is dominated by ν_3, ν_4 and ν_6 vibronic $^2E \rightarrow {}^4A_2$ transitions of Mn^{4+}. However, at 4 K there are no anti-Stokes vibronic emissions as no phonon states are occupied in the ^2E excited state. Because of the D_{3d} site symmetry for Mn^{4+} in $Cs_2HfF_6:Mn^{4+}$, the triply degenerate $\nu_3(T_{1u})$, $\nu_4(T_{1u})$ and $\nu_6(T_{2u})$ modes (in O_h symmetry) split into a singly and a doubly degenerate mode [36,37]. The modes with T_{1u} symmetry split into an A_{2u} and E_u mode and the T_{2u} mode splits into an A_{1u} and E_u mode. At 4 K this splitting is visible in the ν_4 and ν_6 emissions but not observed in the ν_3 peak, where it can be obscured due to broadening of the individual A_{2u} and E_u emission lines.

From the emission spectrum we determine the energies of the asymmetric vibrational modes. The results are summarized in Table 1. The vibrational frequencies found for $Cs_2HfF_6:Mn^{4+}$ are very similar to those reported for Cs_2MnF_6 by Chodos et al. [40], which for comparison have also been listed in Table 1. Besides the intense ν_3, ν_4 and ν_6 peaks, several other weak vibronic emissions are present in the emission spectrum of $Cs_2HfF_6:Mn^{4+}$ (see Fig. S2). The weak emission lines between 620 and 630 nm are assigned to coupling with rotatory or translatory lattice modes [37]. The emission line at 642 nm (514 cm^{-1} relative to the ZPL) is attributed to the symmetric $\nu_2(E_g)$ mode of the MnF_6^{2-} group, as this mode has an energy of ~ 500 cm^{-1} in Cs_2MnF_6 and other Mn^{4+}-doped fluorides [16,40]. Furthermore, all peaks at wavelengths longer than 650 nm are ascribed to combinations of the ν_3 mode with other vibrational modes [17]. Emissions due to coupling of the electronic transition with the symmetric (*gerade*) ν_1 and ν_5 modes of the MnF_6^{2-} ion are not observed in the spectrum. The ν_1 and ν_5 modes have energies of ~ 600 and ~ 300 cm^{-1}, respectively [16,40]. As coupling with symmetric modes does not break the parity selection rule, these vibronic lines are expected to be very weak and are therefore probably obscured by the stronger ν_3 and ν_4 peaks.

Table 1
Vibrational mode energies (cm^{-1}) of the MnF_6^{2-} group in $Cs_2HfF_6:Mn^{4+}$ (determined from the vibronic lines in Fig. 4) and Cs_2MnF_6 at T = 4 K. The data of Cs_2MnF_6 is from Ref. [40].

Compound	ν_3	$\nu_4(A_{2u})$	$\nu_4(E_u)$	$\nu_6(A_{1u})$	$\nu_6(E_u)$
$Cs_2HfF_6:Mn^{4+}$	623	318	342	217	243
Cs_2MnF_6	633	332	338	228	

Like the $^2E \rightarrow {}^4A_2$ emission, the $^4A_2 \rightarrow {}^2E$ excitation gains intensity by coupling with asymmetric vibrational modes. The vibrational mode frequencies of the ^2E excited state will be approximately the same as those of the $^4A_2$ ground state. As a consequence, the $^4A_2 \rightarrow {}^2E$ spectrum should be a mirror image of the $^2E \rightarrow {}^4A_2$ emission. The excitation spectrum in Fig. 4 confirms that this is indeed true for $Cs_2HfF_6:Mn^{4+}$. At shorter wavelengths peaks due to $^4A_2 \rightarrow {}^2T_1$ transitions are visible in the excitation spectrum. It is difficult to locate the ZPL of the $^4A_2 \rightarrow {}^2T_1$ transition because of overlap with the stronger vibronic $^4A_2 \rightarrow {}^2E$ excitation lines. We estimate the ZPL to be at 589 nm which gives a $^2T_1$ level energy of 16,978 cm^{-1}.

At higher energies we find the transitions to the Mn^{4+} $^4T_1$ and $^4T_2$ states. A low-temperature spectrum (T = 4 K) of the $^4A_2 \rightarrow {}^4T_1$ and $^4A_2 \rightarrow {}^4T_2$ excitation bands of $Cs_2HfF_6:Mn^{4+}$ is shown in Fig. 5a. At room-temperature these transitions give rise to broad featureless bands (see Fig. 3a), but now at 4 K a well-resolved fine structure is observed in the $^4A_2 \rightarrow {}^4T_2$ excitation band. The $^4A_2 \rightarrow {}^4T_2$ band shows a vibronic progression with an energy spacing of ~500 cm^{-1}. Similar progressions were observed in the $^4A_2 \rightarrow {}^4T_2$ band of $K_2SiF_6:Mn^{4+}$, $K_2TiF_6:Mn^{4+}$ and $K_2GeF_6:Mn^{4+}$ [15,16,34]. There is debate about which vibration is responsible for the vibronic progression in the $^4A_2 \rightarrow {}^4T_2$ band. Adachi et al. ascribe the vibronic progression to the symmetric $\nu_2(E_g)$ mode of the MnF_6^{2-} ion [17,41]. This mode has an energy of 514 cm^{-1} for $Cs_2HfF_6:Mn^{4+}$, which is in good agreement with the progression spacing of ~500 cm^{-1}. Other works however assign the vibronic progression to the symmetric $\nu_1(A_{1g})$ stretching mode [15,16,34]. The energy of the ν_1 mode in the $^4A_2$ ground state is ~600 cm^{-1}, which is somewhat larger than the progression spacing of ~500 cm^{-1}. Paulusz [34] attributes this energy difference to a weakening of the Mn–F bond in the $^4T_2$ excited state due to the presence of an electron in the anti-bonding e_g orbitals [34]. However, the energy difference between the vibrational modes of the ground and excited states is typically much smaller than 100 cm^{-1}. For example, in $MgF_2:Eu^{2+}$ the vibrational frequencies of the Eu^{2+} $4f^6 5d^1$ excited state and $4f^7$ ground state differ only 0–30 cm^{-1} [42]. We therefore assign the vibronic progression in the $^4A_2 \rightarrow {}^4T_2$ band to the ν_2 mode of the MnF_6^{2-} group.

To obtain the energies of the $^4T_1$ and $^4T_2$ states, we have to locate the ZPLs of the $^4A_2 \rightarrow {}^4T_1$ and $^4A_2 \rightarrow {}^4T_2$ transitions. In many works these ZPLs are located by fitting Poisson distributions to the room temperature excitation spectra of Mn^{4+} [17,33,43–47]. This method however gives too low ZPL energies because of thermal broadening of the excitation bands at room temperature [43]. We will therefore instead try to directly observe the ZPLs in a spectral measurement. Since the $^4A_2 \rightarrow {}^4T_{1,2}$ transitions are electric dipole forbidden, the ZPLs have a very low intensity compared to the vibronic $^4A_2 \rightarrow {}^4T_{1,2}$ excitations [16]. The ZPL of the $^4A_2 \rightarrow {}^4T_1$ transition will therefore never be observed as it is always obscured by stronger vibronic $^4A_2 \rightarrow {}^4T_2$ excitations (see Fig. 5a). The ZPL of the lower-energy $^4A_2 \rightarrow {}^4T_2$ transition has however been measured for some compounds by low-temperature high-resolution absorption and two-photon excitation spectroscopy [16,48]. Hence, we recorded a high-resolution spectrum of the low-energy side of the $^4A_2 \rightarrow {}^4T_2$ excitation band, which is shown in Fig. 5b. In the spectrum a small peak is visible at 498.5 nm (20,060 cm^{-1}). Based on previous observations, we assign this peak to the ZPL of the $^4A_2 \rightarrow {}^4T_2$ transition [48].

At wavelengths shorter than the ZPL arise the intense vibronic $^4A_2 \rightarrow {}^4T_2$ excitations. The horizontal bars in Fig. 5b give the energy differences between the ZPL and the vibronic excitation peaks. Similar to the $^2E \rightarrow {}^4A_2$ transition, the $^4A_2 \rightarrow {}^4T_2$ transition can become partly allowed by coupling with asymmetric (*ungerade*) vibrational modes. Hence, we assign the first vibronic peak at 193 cm^{-1} to the $\nu_6(A_{1u})$ mode of the MnF_6^{2-} ion (see also Table 1) [16,49]. By similar reasoning the peaks at 245 and 379 cm^{-1} can be attributed to the $\nu_6(E_u)$ and $\nu_4(E_u)$ asymmetric vibrational modes. Alternatively, splitting of the $^4T_2$ state by the trigonal crystal field may give rise to a second zero-phonon line and therefore the peaks at 245 and 379 cm^{-1} may also correspond

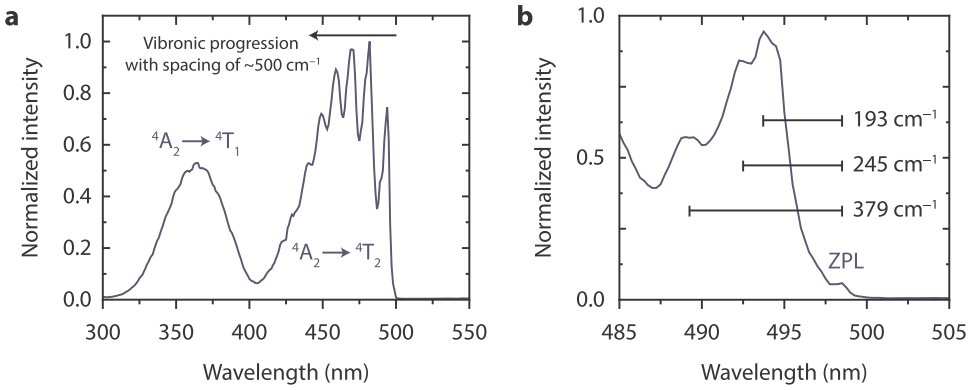

Fig. 5. (a) PL excitation spectrum (λ_{em} = 630 nm) of Cs_2HfF_6:Mn^{4+} at T = 4 K. The $^4A_2 \rightarrow {}^4T_2$ excitation band exhibits a vibronic progression with an energy spacing of ~500 cm^{-1}. (b) High-resolution spectrum of the onset of the $^4A_2 \rightarrow {}^4T_2$ excitation band for Cs_2HfF_6:Mn^{4+}. The horizontal bars indicate the energy differences between the zero-phonon $^4A_2 \rightarrow {}^4T_2$ transition (labeled ZPL) and one-phonon vibronic $^4A_2 \rightarrow {}^4T_2$ excitation peaks.

to vibronic replicas of a second electronic origin. The present spectral data do not allow a definite assignment of the peaks around the onset of the $^4A_2 \rightarrow {}^4T_2$ excitation band. Based on these observations we conclude that the $^4A_2 \rightarrow {}^4T_2$ band structure consists of a ν_2 mode progression of $^4A_2 \rightarrow {}^4T_2 + \nu_u$ transitions, where ν_u is an asymmetric (*ungerade*) vibrational mode in the $^4T_2$ excited state.

The energies we have found for the various Mn^{4+} levels can now be used to determine the crystal field splitting 10 *Dq* (or Δ_O) and Racah parameters *B* and *C*. The Racah parameters (together with *Dq*) provide the energies of all Mn^{4+} states and furthermore give a measure of the nephelauxetic effect [30,39]. The crystal field splitting 10 *Dq* equals the energy of the $^4A_2 \rightarrow {}^4T_2$ transition (see Fig. 3b). In many works on Mn^{4+} and Cr^{3+} the maximum of the $^4A_2 \rightarrow {}^4T_2$ band is therefore taken as the 10 *Dq* energy [15,50–52]. This energy is determined by both the electronic transition energy and the Stokes shift, related to the relaxation in the excited state. An alternative is to use the pure electronic transition energy and to determine the 10 *Dq* value from the energy of the zero-phonon $^4A_2 \rightarrow {}^4T_2$ transition. For Cs_2HfF_6:Mn^{4+} we observed the zero-phonon $^4A_2 \rightarrow {}^4T_2$ transition at 20,060 cm^{-1} and the crystal field splitting 10 *Dq* thus equals this energy. The Racah parameters *B* and *C* can then be obtained with the following relations [36]:

$$\frac{B}{Dq} = \frac{(\Delta E/Dq)^2 - 10(\Delta E/Dq)}{15\left(\frac{\Delta E}{Dq} - 8\right)}, \tag{1}$$

$$\frac{E(^2E)}{B} \cong 3.05\left(\frac{C}{B}\right) + 7.90 - 1.80\left(\frac{B}{Dq}\right). \tag{2}$$

Here ΔE is the energy difference between the $^4T_1$ and $^4T_2$ states and $E(^2E)$ is the ZPL energy of the $^2E \rightarrow {}^4A_2$ transition. As we did not observe the ZPL of the $^4A_2 \rightarrow {}^4T_1$ transition, we estimate ΔE by taking the energy difference between the centers of the $^4A_2 \rightarrow {}^4T_1$ and $^4A_2 \rightarrow {}^4T_2$ excitation bands (centers at 364 and 474 nm, ΔE = 6375 cm^{-1}). It is a good assumption that this difference equals the energy gap between the ZPLs because the Stokes shift will be approximately similar for these transitions. With Eqs. (1) and (2) we then find that B = 601 cm^{-1} and C = 3825 cm^{-1} for Cs_2HfF_6:Mn^{4+}. For comparison, we also calculate the Racah parameters with the maximum of the $^4A_2 \rightarrow {}^4T_2$ band as the 10 *Dq* energy. With this other 10 *Dq* energy we obtain almost similar *B* and *C* values of 596 cm^{-1} and 3832 cm^{-1}, respectively. The *B* and *C* parameters we find for Cs_2HfF_6:Mn^{4+} are in good agreement with those reported for other Mn^{4+}-doped fluorides [39]. Finally, with the *B* and *C* values we can determine the β_1 parameter for Cs_2HfF_6:Mn^{4+}. This parameter was recently introduced by Brik and Srivastava [53] and quantitatively describes the nephelauxetic effect for Mn^{4+}. The β_1 parameter is defined as follows,

$$\beta_1 = \sqrt{\left(\frac{B}{B_0}\right)^2 + \left(\frac{C}{C_0}\right)^2} \tag{3}$$

where B_0 and C_0 are the free ion Racah parameters. For Mn^{4+}, B_0 = 1160 cm^{-1} and C_0 = 4303 cm^{-1} [53]. By using Eq. (3) we determine that β_1 = 1.03 for Cs_2HfF_6:Mn^{4+}. This is a β_1 value typically found for Mn^{4+} in fluorides [39].

3.4. Temperature-dependent luminescence properties

In most phosphor-converted LED systems the phosphor operating temperature is far above room temperature. For example, in high-power 5 W LEDs the temperature near the LED chip can rise to 450 K [5]. It is therefore important to study the thermal quenching behavior of potential LED phosphors. The thermal quenching of the Mn^{4+} emission in Cs_2HfF_6:Mn^{4+} was investigated by measuring the Mn^{4+} emission lifetime (Fig. 6a) and integrated PL intensity (Fig. 6b) as a function of temperature between 4 and 550 K.

The Mn^{4+} emission lifetime shows a steady decrease, starting above 50 K. The decrease in lifetime starts to level off between 200 and 300 K but then shows a rapid decrease above 350 K. To understand the peculiar temperature dependence of the Mn^{4+} emission lifetime, we first

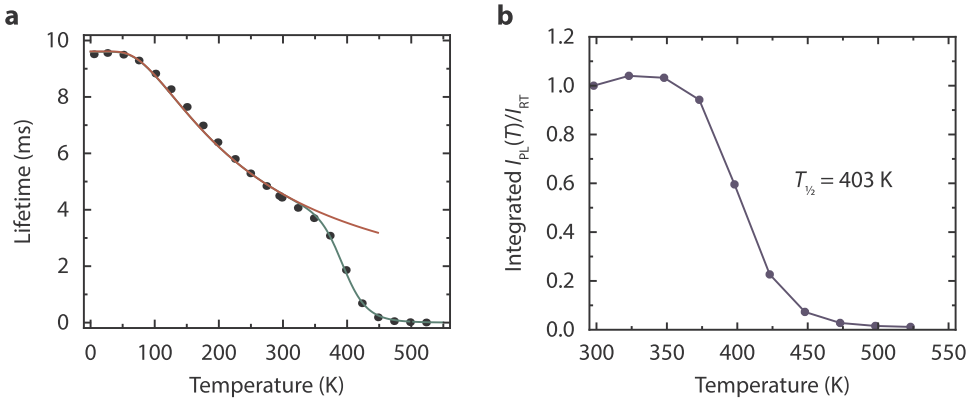

Fig. 6. (a) Temperature dependence of the Mn^{4+} emission lifetime in Cs_2HfF_6:Mn^{4+}. The solid red and green lines represent plots of Eqs. (6) and (7) respectively. (b) Integrated PL intensity of Cs_2HfF_6:Mn^{4+} (λ_{exc} = 470 nm) as a function of temperature. The luminescence quenching temperature $T_{½}$ is 403 K. (For interpretation of the references to color in this figure legend, the reader is referred to the web version of this article.).

look at how the radiative decay rate of the ^2E state changes with temperature. The $^2E \rightarrow {}^4A_2$ emission consists mainly of anti-Stokes and Stokes vibronic emissions. The transition probabilities of these vibronic emissions scale with the phonon occupation number n for anti-Stokes vibronics and $(1 + n)$ for Stokes vibronics. As a consequence, the temperature dependence of the ^2E radiative lifetime τ_R is given by [36],

$$\tau_R(T) = \frac{\tau_R(0)}{2n+1}, \quad (4)$$

with the phonon occupation number n increasing with temperature according to,

$$n = \frac{1}{\exp(h\nu/k_B T)-1}. \quad (5)$$

In Eqs. (4) and (5) $\tau_R(0)$ is the radiative lifetime at $T = 0$ K, k_B is the Boltzmann constant and $h\nu$ is the energy of the phonon coupling to the $^2E \rightarrow {}^4A_2$ transition. If Eqs. (4) and (5) are combined it follows that τ_R can be expressed as,

$$\tau_R(T) = \frac{\tau_R(0)}{\coth(h\nu/2k_B T)}. \quad (6)$$

In Fig. 6a we plot Eq. (6) (solid red line) for $\tau_R(0) = 9.4$ ms and $h\nu = 215$ cm^{-1} (phonon energy of the intense ν_6 mode emission). It can be seen that Eq. (6) describes the temperature dependence of the Mn^{4+} emission lifetime up to 300 K, confirming that the decay of the ^2E state is mainly radiative up to this temperature. The present (simple) model assuming coupling with one dominant vibrational mode gives a good description of the experimentally observed decrease in decay time between 4 and 300 K. The model could be refined by including all three asymmetric modes, weighed for the relative intensities of the vibronic lines to account for the difference in coupling strength. In addition, the energy difference between the ^2E and $^4T_2$ state shows a small variation with temperature. This can also affect the lifetime due to partial lifting of the spin selection rule by enhanced admixture of the $^4T_2$ state through spin-orbit coupling when the ^2E-$^4T_2$ gap becomes smaller. These effects can be neglected in first approximation and it is clear that the decrease in lifetime up to 300 K is caused by an increase in the radiative decay rate for the Stokes and anti-Stokes vibronic lines. There is no thermal quenching of the emission up to 300 K.

Above 350 K the Mn^{4+} emission lifetime is shorter than predicted by Eq. (6) (see Fig. 6a). This difference is explained by the onset of non-radiative transitions. The non-radiative transition probability quickly increases with temperature above 350 K and as a consequence the luminescence of Cs_2HfF_6:Mn^{4+} is quenched. This is confirmed by measurements of the integrated PL intensity, shown in Fig. 6b. The integrated PL intensity of Cs_2HfF_6:Mn^{4+} is relatively constant up to 350 K but rapidly decreases above this temperature with no luminescence remaining at 550 K. The data shown in Fig. 6b are consistent with the temperature-dependent PL intensity previously reported for Cs_2HfF_6:Mn^{4+} [26]. The luminescence quenching temperature $T_{½}$, the temperature at which the PL intensity is half of its room-temperature value, is determined to be 403 K (130 °C). Due to the luminescence quenching above 100 °C, application of Cs_2HfF_6:Mn^{4+} will be limited to low-power LED systems. To determine the activation energy of the thermal quenching process, we fitted the data in Fig. 6a with the following expression [54],

$$\tau(T) = \frac{\tau_R(T)}{1 + \left(\frac{\tau_R(T)}{\tau_{NR}}\right)\mathrm{Exp}(-\Delta E/k_B T)}, \quad (7)$$

where ΔE is the activation energy of the thermal quenching process and τ_{NR} is the non-radiative decay time. From the fit with Eq. (7) (green line in Fig. 6a) we obtain an activation energy ΔE of 6322 cm^{-1}. The mechanism for temperature quenching of Mn^{4+} emission in fluoride hosts will be discussed in a future article.

4. Conclusion

A new class of Mn^{4+}-doped narrow band red emitting phosphors is introduced: Mn^{4+}-doped fluorohafnates. Single phase Cs_2HfF_6:Mn^{4+} phosphor was prepared via a simple two-step co-precipitation method. ICP-OES measurements confirmed that the Mn^{4+} ions are effectively incorporated into the Cs_2HfF_6 host. Under blue photoexcitation Cs_2HfF_6:Mn^{4+} shows bright narrow red Mn^{4+} luminescence that is centered around 620 nm. We have accurately determined the energies of the Mn^{4+} states and MnF_6^{2-} vibrational modes in Cs_2HfF_6:Mn^{4+} from emission and excitation spectra recorded at 4 K. The phosphor exhibits high photoluminescence quantum efficiencies of 80–90% and this combined with the narrow red luminescence under blue light excitation makes Cs_2HfF_6:Mn^{4+} an interesting material for LED applications. Cs_2HfF_6:Mn^{4+} can however only be used in low-power LED systems as its luminescence is quenched above 100 °C ($T_{½}$ = 403 K). In addition, the availability and price of hafnium oxide need to be considered for the large scale production of this phosphor. As the amount of phosphor in wLEDs is very small (~1 mg per wLED) the total amount of phosphor is very low (100 times less material is used in comparison to fluorescent tubes for light generation). Based on this and the abundance of Hf in the earths' crust (similar to that of lanthanides as Eu presently used in lighting), phosphors based on Hf will not cause a significant increase in the price of wLEDs.

Acknowledgements

We thank Stephan Zevenhuizen for performing the SEM and EDX measurements. Mart Peeters is acknowledged for measuring the PL quantum efficiencies. This work is financially supported by Technologiestichting STW (12741), which is part of the Nederlandse Organisatie voor Wetenschappelijk Onderzoek (NWO).

Appendix A. Supporting information

Supplementary data associated with this article can be found in the online version at http://dx.doi.org/10.1016/j.jlumin.2017.10.006.

References

[1] Charge of the LED brigade: A global switch to LEDs will change the lighting business, The Economist, 2011.
[2] M.R. Krames, O.B. Shchekin, R. Mueller-Mach, G.O. Mueller, L. Zhou, G. Harbers, M.G. Craford, Status and future of high-power light-emitting diodes for solid-state lighting, IEEE/OSA J. Disp. Technol. 3 (2007) 160–175, http://dx.doi.org/10.1109/JDT.2007.895339.
[3] G. Harbers, S.J. Bierhuizen, M.R. Krames, Performance of high power light emitting diodes in display illumination applications, IEEE/OSA J. Disp. Technol. 3 (2007) 98–109, http://dx.doi.org/10.1109/JDT.2007.894384.
[4] A.A. Setlur, Phosphors for LED-based solid-state lighting, Electrochem. Soc. Interface 18 (2009) 32–36.
[5] P.F. Smet, A.B. Parmentier, D. Poelman, Selecting conversion phosphors for white light-emitting diodes, J. Electrochem. Soc. 158 (2011) R37–R54, http://dx.doi.org/10.1149/1.3568524.
[6] V. Bachmann, C. Ronda, A. Meijerink, Temperature quenching of yellow Ce^{3+} luminescence in YAG:Ce, Chem. Mater. 21 (2009) 2077–2084, http://dx.doi.org/10.1021/cm8030768.
[7] A.A. Setlur, E.V. Radkov, C.S. Henderson, J.-H. Her, A.M. Srivastava, N. Karkada, M.S. Kishore, N.P. Kumar, D. Aesram, A. Deshpande, B. Kolodin, L.S. Grigorov, U. Happek, Energy-efficient, high-color-rendering LED lamps using oxyfluoride and fluoride phosphors, Chem. Mater. 22 (2010) 4076–4082, http://dx.doi.org/10.1021/cm100960g.
[8] S. Ye, F. Xiao, Y.X. Pan, Y.Y. Ma, Q.Y. Zhang, Phosphors in phosphor-converted white light-emitting diodes: Recent advances in materials, techniques and properties, Mater. Sci. Eng. R Rep. 71 (2010) 1–34, http://dx.doi.org/10.1016/j.mser.2010.07.001.
[9] K. Uheda, N. Hirosaki, Y. Yamamoto, A. Naito, Luminescence properties of a red phosphor, $CaAlSiN_3$:Eu^{2+}, for white light-emitting diodes, Electrochem. Solid-State Lett. 9 (2006) H22–H25, http://dx.doi.org/10.1149/1.2173192.
[10] P. Pust, A.S. Wochnik, E. Baumann, P.J. Schmidt, D. Wiechert, C. Scheu, W. Schnick, $Ca[LiAl_3N_4]$:Eu^{2+} – a narrow-band red-emitting nitridolithoaluminate, Chem. Mater. 26 (2014) 3544–3549, http://dx.doi.org/10.1021/cm501162n.
[11] P. Pust, V. Weiler, C. Hecht, A. Tücks, A.S. Wochnik, A.-K. Henß, D. Wiechert,

C. Scheu, P.J. Schmidt, W. Schnick, Narrow-band red-emitting $Sr[LiAl_3N_4]:Eu^{2+}$ as a next-generation LED-phosphor material, Nat. Mater. 13 (2014) 891–896, http://dx.doi.org/10.1038/nmat4012.
[12] C. Hecht, F. Stadler, P.J. Schmidt, V. Baumann, W. Schnick, $SrAlSi_4N_7:Eu^{2+}$ – a nitridoalumosilicate phosphor for warm white light (pc)LEDs with edge-sharing tetrahedra, Chem. Mater. 21 (2009) 1595, http://dx.doi.org/10.1021/cm803233d.(21).
[13] S. Schmiechen, H. Schneider, P. Wagatha, C. Hecht, P.J. Schmidt, W. Schnick, Toward new phosphors for application in illumination-grade white pc-LEDs: the nitridomagnesosilicates $Ca[Mg_3SiN_4]:Ce^{3+}$, $Sr[Mg_3SiN_4]:Eu^{2+}$, and $Eu[Mg_3SiN_4]$, Chem. Mater. 26 (2014) 2712–2719, http://dx.doi.org/10.1021/cm500610v.
[14] R.J. Xie, N. Hirosaki, Silicon-based oxynitride and nitride phosphors for white LEDs-A review, Sci. Technol. Adv. Mater. 8 (2007) 588–600, http://dx.doi.org/10.1016/j.stam.2007.08.005.
[15] H. Zhu, C.C. Lin, W. Luo, S. Shu, Z. Liu, Y. Liu, J. Kong, E. Ma, Y. Cao, R.-S. Liu, X. Chen, Highly efficient non-rare-earth red emitting phosphor for warm white light-emitting diodes, Nat. Commun. 5 (2014) 4312, http://dx.doi.org/10.1038/ncomms5312.
[16] L. Helmholz, M.E. Russo, Spectra of manganese(IV) hexafluoride ion (MnF_6^{2-}) in environments of O_h and D_{3d} symmetry, J. Chem. Phys. 59 (1973) 5455–5470, http://dx.doi.org/10.1063/1.1679896.
[17] T. Takahashi, S. Adachi, Mn^{4+}-activated red photoluminescence in K_2SiF_6 phosphor, J. Electrochem. Soc. 155 (2008) E183, http://dx.doi.org/10.1149/1.2993159.
[18] M.G. Brik, A.M. Srivastava, On the optical properties of the Mn^{4+} ion in solids, J. Lumin. 133 (2013) 69–72, http://dx.doi.org/10.1016/j.jlumin.2011.08.047.
[19] C.C. Lin, A. Meijerink, R.-S. Liu, Critical red components for next-generation white LEDs, J. Phys. Chem. Lett. 7 (2016) 495–503, http://dx.doi.org/10.1021/acs.jpclett.5b02433.
[20] J.E. Murphy, F. Garcia-Santamaria, A.A. Setlur, S. Sista, PFS, $K_2SiF_6:Mn^{4+}$: the red-line emitting LED phosphor behind GE's TriGain Technology™ platform, SID Symp. Dig. Tech. Pap. 46 (2015) 927–930, http://dx.doi.org/10.1002/sdtp.10406.
[21] L.-L. Wei, C.C. Lin, M.-H. Fang, M.G. Brik, S.-F. Hu, H. Jiao, R.-S. Liu, A low-temperature co-precipitation approach to synthesize fluoride phosphors $K_2MF_6:Mn^{4+}$ (M = Ge, Si) for white LED applications, J. Mater. Chem. C 3 (2015) 1655–1660, http://dx.doi.org/10.1039/C4TC02551B.
[22] S. Adachi, T. Takahashi, Direct synthesis and properties of $K_2SiF_6:Mn^{4+}$ phosphor by wet chemical etching of Si wafer, J. Appl. Phys. 104 (2008) 23512, http://dx.doi.org/10.1063/1.2956330.
[23] Y. Arai, S. Adachi, Optical properties of Mn^{4+}-activated Na_2SnF_6 and Cs_2SnF_6 red phosphors, J. Lumin. 131 (2011) 2652–2660, http://dx.doi.org/10.1016/j.jlumin.2011.06.042.
[24] H.-D. Nguyen, R.-S. Liu, Narrow-band red-emitting Mn^{4+}-doped hexafluoride phosphors: synthesis, optoelectronic properties, and applications in white light-emitting diodes, J. Mater. Chem. C 4 (2016) 10759–10775, http://dx.doi.org/10.1039/C6TC03292C.
[25] Y. Zhu, L. Huang, R. Zou, J. Zhang, J. Yu, M. Wu, J. Wang, Q. Su, Hydrothermal synthesis, morphology and photoluminescent properties of an Mn^{4+}-doped novel red fluoride phosphor elpasolite K2LiAlF6, J. Mater. Chem. C 4 (2016) 5690–5695, http://dx.doi.org/10.1039/C6TC01366J.
[26] Z. Yang, Q. Wei, M. Rong, Z. Yang, Z. Wang, Q. Zhou, Q. Wang, Novel red-emitting phosphors $A_2\ HfF_6:Mn^{4+}$ (A = Rb^+, Cs^+) for solid-state lighting, Dalton Trans. 46 (2017) 9451–9456, http://dx.doi.org/10.1039/C7DT01842H.
[27] H. Bode, H. Jenssen, F. Bandte, Über eine neue darstellung des kalium-hexa-fluoromanganats(IV), Angew. Chem. 65 (1953) 304, http://dx.doi.org/10.1002/ange.19530651108.
[28] H.W. Roesky, Efficient Preparations of Fluorine Compounds, John Wiley & Sons, Inc, Hoboken, NJ, USA, 2012, http://dx.doi.org/10.1002/9781118409466.
[29] H. Bode, G. Teufer, Über strukturen von hexafluorozirkonaten und hexa-fluorohafnaten, Z. Anorg. Allg. Chem. 283 (1956) 18–25, http://dx.doi.org/10.1002/zaac.19562830105.
[30] Y. Tanabe, S. Sugano, On the absorption spectra of complex ions. I, J. Phys. Soc. Jpn. 9 (1954) 753–766, http://dx.doi.org/10.1143/JPSJ.9.753.
[31] Y. Tanabe, S. Sugano, On the absorption spectra of complex ions II, J. Phys. Soc. Jpn. 9 (1954) 766–779, http://dx.doi.org/10.1143/JPSJ.9.766.
[32] M. de Jong, L. Seijo, A. Meijerink, F.T. Rabouw, Resolving the ambiguity in the relation between Stokes shift and Huang–Rhys parameter, Phys. Chem. Chem. Phys. 17 (2015) 16959–16969, http://dx.doi.org/10.1039/C5CP02093J.
[33] Y.K. Xu, S. Adachi, Properties of Mn^{4+}-activated hexafluorotitanate phosphors, J. Electrochem. Soc. 158 (2011) J58, http://dx.doi.org/10.1149/1.3530793.
[34] A.G. Paulusz, Efficient Mn(IV) emission in fluorine coordination, J. Electrochem. Soc. 120 (1973) 942–947, http://dx.doi.org/10.1149/1.2403605.
[35] T. Senden, F.T.H. Broers, A. Meijerink, Comparative study of the Mn^{4+} $^2E \rightarrow {}^4A_2$ luminescence in isostructural $RE_2Sn_2O_7:Mn^{4+}$ pyrochlores (RE^{3+} = Y^{3+}, Lu^{3+} or Gd^{3+}), Opt. Mater. 60 (2016) 431–437, http://dx.doi.org/10.1016/j.optmat.2016.08.024.
[36] B. Henderson, G.F. Imbusch, Optical Spectroscopy of Inorganic Solids, Oxford University Press, Oxford, 1989.
[37] I.W. Forrest, A.P. Lane, Single-crystal polarized infrared and Raman spectra and normal-coordinate analysis of some Group 4 complex hexafluorometalates, Inorg. Chem. 15 (1976) 265–269, http://dx.doi.org/10.1021/ic50156a004.
[38] R.D. Shannon, Revised effective ionic radii and systematic studies of interatomic distances in halides and chalcogenides, Acta Crystallogr. Sect. A 32 (1976) 751–767, http://dx.doi.org/10.1107/S0567739476001551.
[39] M.G. Brik, S.J. Camardello, A.M. Srivastava, Influence of covalency on the Mn^{4+} $^2E_g \rightarrow {}^4A_{2g}$ emission energy in crystals, ECS J. Solid State Sci. Technol. 4 (2014) R39–R43, http://dx.doi.org/10.1149/2.0031503jss.
[40] S.L. Chodos, A.M. Black, C.D. Flint, Vibronic spectra and lattice dynamics of Cs_2MnF_6 and $A_2^IM^{IV}F_6:MnF_6^{2-}$, J. Chem. Phys. 65 (1976) 4816–4824, http://dx.doi.org/10.1063/1.432952.
[41] D. Sekiguchi, J. Nara, S. Adachi, Photoluminescence and Raman scattering spectroscopies of $BaSiF_6:Mn^{4+}$ red phosphor, J. Appl. Phys. 113 (2013) 183516, http://dx.doi.org/10.1063/1.4803880.
[42] S. Lizzo, A.H. Velders, A. Meijerink, G.J. Dirksen, G. Blasse, The luminescence of Eu^{2+} in magnesium fluoride crystals, J. Lumin. 65 (1995) 303–311, http://dx.doi.org/10.1016/0022-2313(95)00080-1.
[43] Y. Arai, S. Adachi, Optical transitions and internal vibronic frequencies of MnF_6^{2-} ions in Cs_2SiF_6 and Cs_2GeF_6 red phosphors, J. Electrochem. Soc. 158 (2011) J179, http://dx.doi.org/10.1149/1.3576124.
[44] Y.K. Xu, S. Adachi, Properties of $Na_2SiF_6:Mn^{4+}$ and $Na_2GeF_6:Mn^{4+}$ red phosphors synthesized by wet chemical etching, J. Appl. Phys. 105 (2009) 13525, http://dx.doi.org/10.1063/1.3056375.
[45] S. Adachi, T. Takahashi, Photoluminescent properties of $K_2GeF_6:Mn^{4+}$ red phosphor synthesized from aqueous $HF/KMnO_4$ solution, J. Appl. Phys. 106 (2009) 13516, http://dx.doi.org/10.1063/1.3160303.
[46] D. Sekiguchi, S. Adachi, Synthesis and optical properties of $BaTiF_6:Mn^{4+}$ red phosphor, ECS J. Solid State Sci. Technol. 3 (2014) R60–R64, http://dx.doi.org/10.1149/2.025404jss.
[47] S. Sakurai, T. Nakamura, S. Adachi, $Rb_2SiF_6:Mn^{4+}$ and $Rb_2TiF_6:Mn^{4+}$ red-emitting phosphors, ECS J. Solid State Sci. Technol. 5 (2016) R206–R210, http://dx.doi.org/10.1149/2.0171612jss.
[48] C. Campochiaro, D.S. McClure, P. Rabinowitz, S. Dougal, Vibronic coupling in the two-photon $^4A_2 \rightarrow {}^4T_2$ spectrum of Mn^{4+} in the cubic and trigonal sites of Cs_2MF_6, M = Si, Ge, Ti, Chem. Phys. Lett. 157 (1989) 78–82, http://dx.doi.org/10.1016/0009-2614(89)87211-2.
[49] M.J. Reisfeld, N.A. Matwiyoff, L.B. Asprey, The electronic spectrum of cesium hexafluoromanganese(IV), J. Mol. Spectrosc. 39 (1971) 8–20, http://dx.doi.org/10.1016/0022-2852(71)90270-0.
[50] B. Wang, H. Lin, J. Xu, H. Chen, Y. Wang, $CaMg_2Al_{16}O_{27}:Mn^{4+}$-based red phosphor: a potential color converter for high-powered warm W-led, ACS Appl. Mater. Interfaces 6 (2014) 22905–22913, http://dx.doi.org/10.1021/am507316b.
[51] V. Singh, R.P.S. Chakradhar, J.L. Rao, H.Y. Kwak, EPR and photoluminescence properties of combustion-synthesized $ZnAl_2O_4:Cr^{3+}$ phosphors, J. Mater. Sci. 46 (2011) 2331–2337, http://dx.doi.org/10.1007/s10853-010-5078-z.
[52] L. Zhang, L. Li, Y. Huang, S. Sun, Z. Lin, G. Wang, Growth, spectral property and crystal field analysis of Cr^{3+}-doped $Na_2Mg_5(MoO_4)_6$ crystal, Opt. Mater. 49 (2015) 75–78, http://dx.doi.org/10.1016/j.optmat.2015.08.022.
[53] A.M. Srivastava, M.G. Brik, Crystal field studies of the Mn^{4+} energy levels in the perovskite, LaAlO3, Opt. Mater. 35 (2013) 1544–1548, http://dx.doi.org/10.1016/j.optmat.2013.03.021.
[54] A.M. Srivastava, H.A. Comanzo, S. Camardello, S.B. Chaney, M. Aycibin, U. Happek, Unusual luminescence of octahedrally coordinated divalent europium ion in $Cs_2M^{2+}P_2O_7$ (M^{2+} = Ca, Sr), J. Lumin. 129 (2009) 919–925, http://dx.doi.org/10.1016/j.jlumin.2009.03.018.